

The influence of shape on the glassy dynamics of hard nonspherical particle fluids. I. Dynamic crossover and elasticity

Cite as: J. Chem. Phys. **130**, 244906 (2009); <https://doi.org/10.1063/1.3157279>

Submitted: 21 February 2009 • Accepted: 30 May 2009 • Published Online: 29 June 2009

Mukta Tripathy and Kenneth S. Schweizer



View Online



Export Citation

ARTICLES YOU MAY BE INTERESTED IN

[The influence of shape on the glassy dynamics of hard nonspherical particle fluids. II. Barriers, relaxation, fragility, kinetic vitrification, and universality](#)

The Journal of Chemical Physics **130**, 244907 (2009); <https://doi.org/10.1063/1.3157280>

[Entropic barriers, activated hopping, and the glass transition in colloidal suspensions](#)

The Journal of Chemical Physics **119**, 1181 (2003); <https://doi.org/10.1063/1.1578632>

[The effect of surface roughness on the phase behavior of colloidal particles](#)

The Journal of Chemical Physics **152**, 044902 (2020); <https://doi.org/10.1063/1.5136080>

Learn More

The Journal of Chemical Physics **Special Topics** Open for Submissions

The influence of shape on the glassy dynamics of hard nonspherical particle fluids. I. Dynamic crossover and elasticity

Mukta Tripathy and Kenneth S. Schweizer^{a)}

Department of Chemical and Biomolecular Engineering and Department of Materials Science, Frederick Seitz Materials Research Laboratory, University of Illinois, 1304 West Green Street, Urbana, Illinois 61801, USA

(Received 21 February 2009; accepted 30 May 2009; published online 29 June 2009)

We extend and apply the center-of-mass version of the microscopic naïve mode coupling theory to study the ideal kinetic glass transition of dense fluids and suspensions composed of broad families of one-, two-, and three- dimensional hard nonspherical particles. A kinetic arrest diagram is constructed which indicates a dynamical crossover or onset of activated barrier hopping controlled transport. We find (quasi-) one-dimensional rods and rings form ideal glasses at the lowest volume fractions which decrease strongly with aspect ratio. Two-dimensional disks form ideal glasses at intermediate volume fractions which decrease slowly with the number of particles comprising the planar objects. Compact three-dimensional cluster particles exhibit a subtle nonmonotonic variation of the onset volume fraction that depends on their detailed shape, surface corrugation, and intraparticle interstitial volume. A strong correlation between the ideal kinetic arrest volume fraction and dimensionless compressibility (amplitude of density fluctuations) is predicted. The elastic shear modulus (transient localization length) grows (decreases) exponentially with volume fraction in a manner that becomes stronger as particle dimensionality increases. © 2009 American Institute of Physics. [DOI: [10.1063/1.3157279](https://doi.org/10.1063/1.3157279)]

I. INTRODUCTION

Glassy dynamics and kinetic structural arrest is a ubiquitous phenomenon in thermal liquids (metal, ceramic, molecular, ionic), colloidal and nanoparticle suspensions, amorphous polymer plastics, and even biological systems such as folded proteins and the crowded cell interior.¹ There has been intense theoretical and simulation activity in this area over the past decade or two. However, with few exceptions, these studies have either adopted (highly) coarse-grained models, or focused on fluids composed of spherical objects such as repulsive or attractive particles or binary Lennard-Jones mixtures. In reality, the large majority of glass-forming materials involve more complex elementary constituents, the most generic aspect of which is nonspherical particle shape. For example, molecular liquids can consist of linear (e.g., alcohols and alkanes), planar (e.g., decalin and trisnaphthylbenzene), or irregularly shaped three-dimensional (3D) molecules. A similar diversity exists at the nanometer and colloidal scales where large aspect ratio disks, rods, ellipsoids, and spherocylinders are classic anisomeric objects. Recently advances in materials science²⁻⁴ have led to the creation of a vast array of nonspherical colloids and nanoparticles of one-dimensional (1D) (e.g., analogs of diatomic and triatomic molecules), two-dimensional (2D) (e.g., triangles and planar structures), and 3D cluster (e.g., cubes, tetrahedra, and octahedra) objects. Besides the intrinsic interest of slow dynamics in such systems, understanding diffusion and flow under glassy conditions is also relevant to equilibrium self-assembly² and crystal nucleation and growth.^{5,6}

Until very recently, microscopic theoretical work on dense fluids of nonspherical particles was limited to ideal mode coupling theory^{7,8} studies of hard core ellipsoids⁹ and homonuclear diatomics.¹⁰ Complementary computer simulations of hard ellipsoids¹¹ and diatomics¹² have also been performed that establish the effect of the aspect ratio of uniaxial objects on the onset of slow glassy dynamics. The goal of the present and following companion article [referred to as paper II (Ref. 13)] is to build on our recent progress in developing a first principles theory for the activated dynamics of fluids and suspensions of hard spheres^{14,15} and uniaxial objects¹⁶ in order to treat systems composed of a wide variety of shapes. The focus is on the most generic aspect: Newtonian fluids (ignoring inertial effects) and overdamped suspensions (ignoring long range hydrodynamics) composed of rigid objects that interact solely via excluded volume forces. The goal of this first paper is to establish how particle shape determines the ideal kinetic arrest diagram which represents the onset of activated glassy behavior. Properties determined by small scale physics, such as the transient localization length and elastic shear modulus, are also studied. In the following companion paper II, the entropic barriers, alpha relaxation time, and self-diffusion constant in the activated hopping regime are determined. The question of how shape determines “dynamic fragility” and *kinetic* vitrification is investigated. It is shown that fluids of nonspherical hard objects display a remarkably wide variation in the sensitivity of their relaxation time to volume fraction. A nearly universal picture is developed for all shapes which predicts the entropic barrier for diffusive transport and relaxation is controlled by a mean square force exerted on a tagged particle determined prima-

^{a)}Electronic mail: kschweiz@illinois.edu.

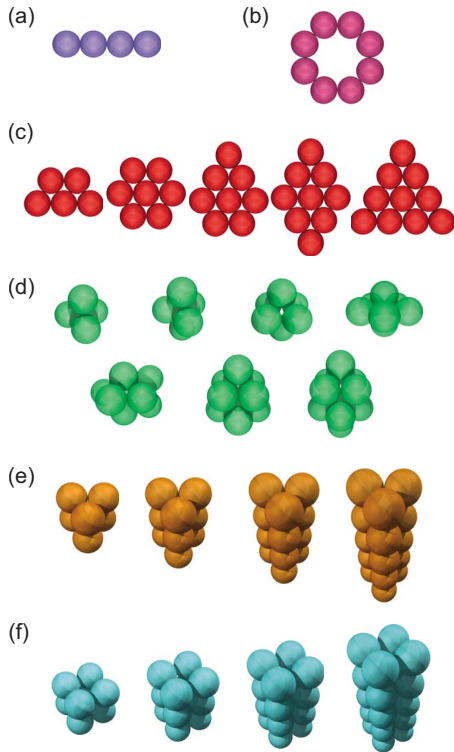


FIG. 1. (Color online) Examples of the five families of shapes studied. (a) The 1D four-site rod. (b) The eight-site ring. (c) From left to right, the two-dimensional disks of $N=5, 7, 8, 9,$ and 10 sites. (d) Compact 3D Conway particles. Top row: from left to right, the tetrahedron, triangular dipyramid, octahedron, and pentagonal dipyramid. Bottom row: from left to right, the snub disphenoid, gyroelongated square pyramid, and gyroelongated square dipyramid. (e) Triangle family. From left to right, the triangular prism, triply stacked triangles, quadruply stacked triangles, and quintuply stacked triangles. (f) Square family. From left to right, the cube, triply stacked squares, quadruply stacked squares, and quintuply stacked squares.

rily by a local structure metric that quantifies interparticle collision rates.^{16,17}

In Sec. II the models and statistical mechanical theories employed in the present and companion paper are summarized. Representative structure calculations are presented in Sec. III, and the naive mode coupling theory (NMCT) kinetic arrest diagram is discussed in Sec. IV. Section V presents calculations of the dynamic free energy, localization length, and shear modulus. The paper concludes in Sec. VI with a summary and discussion. A table of the different shapes studied and several of their characteristic properties is given in the Appendix.

II. THEORY

The basic equilibrium and dynamic theoretical tools employed have been discussed in detail previously.^{14–16} Here we provide a brief summary.

A. Hard particle models

The rigid particles or “objects” studied are clusters of bonded tangent spherical sites (diameter σ) that interact via pair decomposable site-site hard core repulsions.¹⁸ Figure 1 depicts the different particle shapes studied which fall into five families. Two groups of 1D particles are considered: rods and rings (sites placed on vertices of a polygon) of

variable number of sites, N . The two-dimensional particles examined are planar disks where the sites form a subset of the hexagonal lattice. The *maximally compact* 3D shapes are comprised of N spherical sites located on the vertices of polyhedra, all of which have been recently synthesized as colloids via a droplet oil-in-water emulsion technique.³ The clusters formed by the latter method correspond to structures that minimize the second moment of their mass distribution or radius-of-gyration, R_g . These objects are known as “Conway shapes” in recognition of the mathematician who discussed them.¹⁹ The specific Conway shapes studied are tetrahedron, triangular dipyramid, octahedron, pentagonal dipyramid, snub disphenoid, gyroelongated square pyramid, and gyroelongated square dipyramid corresponding to particles with $N=4, 5, 6, 7, 8, 9,$ and 10 sites, respectively.

Two additional classes of *non-Conway* particles are studied which we refer to as the triangle and square families. The former consists of triangles stacked orthogonal to their planes, and the latter consists of similarly stacked squares. The specific shapes studied are triangle, doubly stacked triangles (triangular prism), triply stacked triangles, quadruply stacked triangles, quintuply stacked triangles, and the square, doubly stacked squares (cube), triply stacked squares, quadruply stacked squares, and quintuply stacked squares. These shapes are not maximally compact and have a mixed dimensionality character.

Table I of the Appendix lists key particle properties: radius of gyration, normalized second virial coefficient, and space-filling fraction. The latter two quantities are measures of the strength of the two particle excluded volume interaction and degree of compactness, respectively, and are defined as

$$\tilde{B}_2 = \frac{B_2}{N\pi\sigma^3/6}, \quad (1)$$

$$\phi_{\text{space}} = \frac{N\pi\sigma^3/6}{4\pi R_g^3/3}. \quad (2)$$

The space-filling fraction (\tilde{B}_2) monotonically decreases (increases) as the object effective dimensionality (aspect ratio) grows. There are subtle variations of these two properties among the compact Conway shapes, and the non-Conway shapes are “less dense.”

B. Structural correlations

Equilibrium structure is determined using the reference interaction site model (RISM) theory.¹⁸ Assuming all particle sites are symmetry equivalent (rigorous for the two-site rod, all rings, tetrahedron, octahedron, triangular prism and cube, but an approximation for other shapes), the site-site Chandler–Andersen scalar integral equation in Fourier space is^{16,18}

$$h_{ss}(k) = \omega(k)C_{ss}(k)\omega(k) + \rho_s\omega(k)C_{ss}(k)h_{ss}(k), \quad (3)$$

where $\rho_s=N\rho$ is the site number density, ρ is the molecular number density, $h_{ss}(k)$ is the Fourier transform of the nonrandom part of the site-site pair correlation function,

$h_{ss}(r) = g_{ss}(r) - 1$, $C_{ss}(k)$ is the site-site direct correlation function, and $\omega(k)$ is the intramolecular structure factor

$$\omega(k) = \frac{1}{N} \sum_{\alpha, \gamma=1}^N \frac{\sin r_{\alpha\gamma} k}{r_{\alpha\gamma} k}, \quad (4)$$

which is the Fourier transform of the intramolecular distribution function, $\omega(r) = N^{-1} \sum_{\alpha, \gamma=1}^N \delta(r - r_{\alpha\gamma})$, where $r_{\alpha\gamma}$ is the scalar distance between sites α and γ . All $\omega(k)$ are easily computed,^{19,20} and Eq. (3) is solved using the RISM closure approximation,¹⁸

$$\begin{aligned} C_{ss}(r) &= 0, & r > \sigma, \\ g_{ss}(r) &= 0, & r < \sigma. \end{aligned} \quad (5)$$

The collective density fluctuation structure factor in the site representation is

$$S_{ss}(k) = \omega(k) + \rho_s h_{ss}(k). \quad (6)$$

The glassy dynamics is studied at the center-of-mass (CM) level.¹⁶ In a literal implementation of the CM theory the site-site correlations are related to their CM analogs (denoted by the subscript cc). The so-called rigid particle mapping²¹ is employed corresponding to

$$S_{cc}(k) = \frac{S_{ss}(k)}{\omega(k)} = 1 + \rho H_{cc}(k), \quad (7)$$

$$C_{cc}(k) = N\omega(k)C_{ss}(k), \quad (8)$$

$$H_{cc}(k) = \frac{N}{\omega(k)} h_{ss}(k). \quad (9)$$

The CM mapping corresponds to a dynamical description whereby a particle only translates without rotating. However, the theory retains knowledge of particle shape via $\omega(k)$. The connection between the site and CM levels embodied in Eqs. (7)–(9) has been shown to be quite accurate for rigid rods using Monte Carlo simulation.²² The integral equation is solved numerically using the iterative Picard algorithm.²³

C. Center-of-mass mode coupling and nonlinear Langevin equation theories

The NMCT^{14,16,24} and nonlinear Langevin equation (NLE) theory for fluids of nonspherical particles were initially motivated¹⁶ by a literal CM perspective. This results in a dynamical description of the *same form* as for spherical particles but with Eqs. (7)–(9) as structural input. The scalar particle CM displacement from its initial position, $r(t)$, is the central dynamic variable which obeys a stochastic equation of motion derived using dynamic density functional ideas at a lightly coarse-grained (not ensemble-averaged) level.²⁵ By adopting an average description of caging constraints, and invoking a “local equilibrium approximation” that relates one and two particle dynamics, a closed NLE in the overdamped limit is obtained,^{14,16,25}

$$\zeta_s \frac{d}{dt} r - \frac{\partial}{\partial r} F_{\text{eff}}(r) + \delta f = 0, \quad (10)$$

$$\langle \delta f(0) \delta f(t) \rangle = 2k_B T \zeta_s \delta(t).$$

Here, $\delta f(t)$ is a white noise stochastic force, and $\zeta_s = k_B T / D_s$ (D_s) is the short time friction (diffusion) constant determined in fluids by independent binary collisions or in suspensions by a combination of two body hydrodynamics and binary collisions.¹⁴

The key quantity in Eq. (10) is $F_{\text{eff}}(r)$, an effective or dynamic “free energy,” given by

$$\begin{aligned} \beta F_{\text{eff}}(r) &= -3 \ln(r) \\ &- \int \frac{d\vec{k}}{(2\pi)^3} \rho C_{cc}^2(k) \frac{S_{cc}(k)}{1 + S_{cc}^{-1}(k)} e^{-(k^2 r^2 / 6) [1 + S_{cc}^{-1}(k)]}. \end{aligned} \quad (11)$$

The first term is an ideal entropy-like term which favors the “delocalized” liquid state, whereas the second term is the intermolecular caging contribution that favors transient particle trapping. Equations (10) and (11) predict a dynamic crossover to activated dynamics at a critical volume fraction, ϕ_c , which signals the CM-NMCT ideal glass or kinetic arrest transition. The latter is described by^{14,16} the following self-consistent equation for the long time limit of the ensemble-averaged CM mean square displacement (localization length), $r_{\text{loc}}^2 \equiv \langle r^2(t \rightarrow \infty) \rangle$,

$$\frac{1}{r_{\text{loc}}^2} = \frac{1}{9} \int \frac{d\vec{k}}{(2\pi)^3} \rho k^2 C_{cc}^2(k) S_{cc}(k) e^{-(k^2 r_{\text{loc}}^2 / 6) [1 + S_{cc}^{-1}(k)]}. \quad (12)$$

Beyond ϕ_c , a localization well and barrier emerges in the dynamic free energy.

The main structural input to the NMCT of Eq. (12) is the so-called “vertex”,^{16,17}

$$V(k) \equiv k^4 \rho C_{cc}^2(k) S_{cc}(k) = N k^4 \rho_s \omega(k) C_{ss}^2(k) S_{ss}(k), \quad (13)$$

where the second equality follows from Eqs. (7)–(9). The vertex quantifies the total effective mean square force exerted on a particle by the surrounding fluid. When $V(k)$ is written in the site representation one sees the CM dynamic theory is based on the total force on a tagged molecule at the site level under the assumption that such forces decay in time only via CM motions, corresponding to a dynamically non-rotating approximation.^{16,26} Prior work¹⁶ has shown the reliability of such a conceptual and technical simplification for fluids of hard diatomics, triatomics, spherocylinders and rods, although orientational dynamics is not described. Moreover, the fact that the CM vertex of Eq. (13) is entirely determined by site-site correlations provides support for the accuracy of the structural input given the known reliability of RISM theory for dense fluids of nonspherical particles.¹⁸

All single particle dynamical properties can be calculated by solving the NLE using stochastic trajectory simulation.¹⁵ In the present and companion paper, only the

most basic quantities which can be determined nearly analytically are studied. The elastic shear modulus, G' , is computed based on the standard Green–Kubo formula^{27,28}

$$G' = \frac{k_B T}{60\pi^2} \int_0^\infty dk \left[k^2 \frac{d}{dk} \ln(S_{cc}(k)) \right]^2 e^{-k^2 r_{loc}^2 / 3 S_{cc}(k)}. \quad (14)$$

D. Analytic ultralocal limit

An analytic (“ultralocal”) analysis of the NLE theory has been performed¹⁷ in the high barrier regime where large wavevector vertex contributions dominate and Eq. (13) simplifies to

$$\lim_{k \rightarrow \infty} V(k) = \lambda \cos^2 k. \quad (15)$$

The “coupling constant,” λ , can be interpreted as an effective or renormalized mean square force exerted on a tagged molecule by its surroundings, and is given by

$$\lambda = 96\pi N \phi g_{ss}^2(\sigma) \propto F_B, \quad (16)$$

where $g_{ss}(\sigma)$ is the contact value of the site-site radial distribution function which quantifies hard core binary collisions. The final proportionality indicates the barrier scales linearly with λ . Eq. (16) serves to emphasize that the key structural input to our dynamical theory is the most local measure of intermolecular correlations at the site, not the CM, level. The analytic analysis proves also that the NLE theory predicts a divergent relaxation time (infinite barrier) only in the incompressible random close packing limit.^{17,29} Moreover, a connection between the glassy dynamics in thermalized fluids and Brownian suspensions, and the jamming of granular systems, is suggested based on the most local measure of structure and confinement forces, the contact value of the radial distribution function.^{17,29}

The elastic shear modulus also simplifies in the ultralocal limit as

$$G' \simeq \frac{k_B T}{60\pi^2} \int_0^\infty dk \left[k^2 \frac{d}{dk} (\rho C_{cc}(k)) \right]^2 e^{-k^2 r_{loc}^2 / 3}. \quad (17)$$

Using the high wavevector result,¹⁷

$$\rho C_{cc}(k) \rightarrow 24\phi g_{ss}(\sigma) \frac{\cos(k\sigma)}{(k\sigma)^2}, \quad (18)$$

one obtains through leading order

$$G' \simeq \frac{18}{5\sqrt{\pi}} \frac{\phi k_B T}{N \sigma r_{loc}^2} = \frac{3\sqrt{\pi}}{5} \rho k T \left(\frac{\sigma}{r_{loc}} \right)^2, \quad (19)$$

where $\sin^2(k\sigma) \rightarrow 1/2$ has been used. Hence, the elastic modulus is proportional to the molecular number density, and is inversely proportional to the square of the localization length.

III. FLUID STRUCTURE

Figure 2 shows examples of the site-site radial distribution functions of seven-site particles at a fixed large volume fraction $\phi=0.50$. Since higher dimensional particles are more compact they make fewer contacts with surrounding

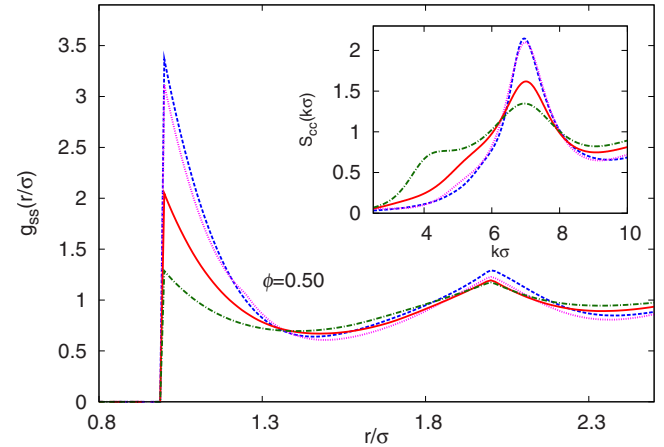


FIG. 2. (Color online) Site-site pair correlation function as a function of reduced site separation for various particles of seven sites at fixed $\phi=0.50$: rod (dashed, blue curve), heptagon (dotted, pink curve), disk (solid red, curve), and pentagonal dipyramid (dotted-dashed, green curve). The inset shows the CM static structure factor of the same shapes.

particles. An important consequence is the radial distribution function at contact [the key quantity in the dynamical coupling constant λ of Eq. (16)] is a decreasing function of particle dimensionality. Figure 2 also shows that since the ring (heptagon) and rod are open (quasi-) 1D objects, their contact values are nearly equal.

The inset of Fig. 2 presents structure factors for the same seven-site particles. The cage peak intensity, $S_{cc}(k^*)$, decreases with object dimensionality, but is a subtle function of particle shape and N within each dimensionality class. Liquid ordering of the compact objects occurs on both the molecular and site length scales. This is illustrated in Fig. 3 where a “prepeak” in $S_{cc}(k\sigma)$ emerges at wavevectors below the primary cage scale peak for an intermediate volume fraction of $\phi=0.35$. The prepeak feature is also present as a weak shoulder for fluids of 1D and two-dimensional shapes (Fig. 2). Figure 3 also demonstrates that as fluids of 3D particles become more dense, the intensity of the primary peak of the structure factor increases, whereas that of the prepeak decreases indicating a shift in ordering length scale from the global object size scale to the site scale.

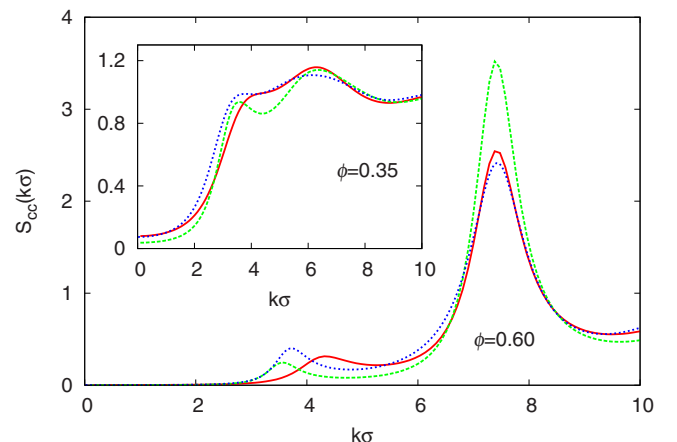


FIG. 3. (Color online) The CM static structure factor of 3D cluster particles: octahedron (solid, red curve), cube (dashed, green curve), and gyroelongated square pyramid (dotted, blue curve) at $\phi=0.60$. The inset plots the CM structure factor of the same shapes at $\phi=0.35$.

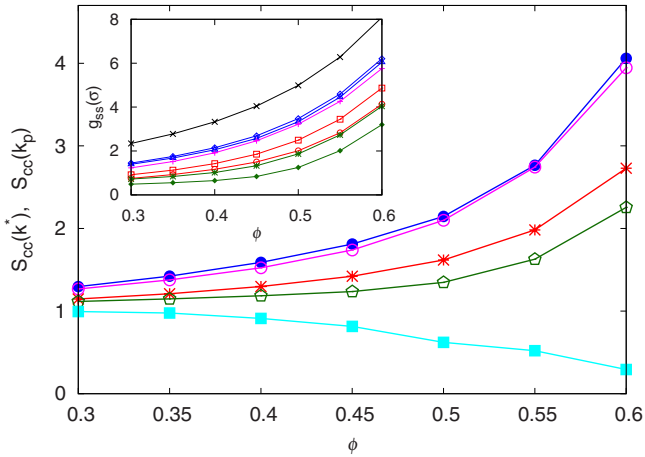


FIG. 4. (Color online) Value of the static structure factor at the cage peak, $S_{cc}(k^*)$, for various seven site particles as a function of volume fraction: rod (solid, blue circles), heptagon (open, pink circles), disk (red asterisks), and pentagonal dipyramid (open, green pentagons). The value of the structure factor at the prepeak/shoulder, $S_{cc}(k_p)$, of the pentagonal dipyramid is also shown (solid, light blue squares). The inset shows the contact value of the site-site radial distribution function for the sphere (black crosses), rod of five sites (open, blue diamonds), rod of eight sites (open, blue triangles), octagon (pink pluses), disk of five sites (open, red squares), disk of eight sites (open, red circles), triangular dipyramid (green asterisks), and snub disphenoid (solid, green diamonds). All curves through the points are guides to the eye.

The effect of volume fraction on the degree of local ordering, as quantified by the intensity of the primary peak and contact value, is presented in Fig. 4 for various seven site shapes; prepeak results for the pentagonal dipyramid fluid are also shown. The contact value generally decreases with increasing number of sites and/or increasing particle dimensionality, but is a more rapidly varying function of volume fraction.

The zero-wavevector limit of the CM structure factor, S_0 , is proportional to the compressibility (κ_T) and amplitude of long wavelength density fluctuations via the relation,

$$S_0 = S_{cc}(k=0) = \rho k_B T \kappa_T = \frac{S_{ss}(k=0)}{N}. \quad (20)$$

Calculations in Fig. 5 show S_0 decreases rapidly with volume fraction, tends to increase with particle dimensionality at fixed ϕ , and decreases with number of sites for rods, rings, and disks at fixed volume fraction. Qualitatively, these trends all correlate with the degree of particle compactness as quantified by ϕ_{space} in Table I (see Appendix). In contrast, S_0 of 3D particles at $\phi=0.35$ display a nonmonotonic variation with N indicating a more highly shape-dependent behavior. As ϕ increases from 0.35 to 0.60, the N -dependence of S_0 changes qualitatively, and we find (not shown) that S_0 at high volume fractions is controlled by a geometric quantity, $\chi = 1 - v$, where v is the “interstitial volume” per site which refers to the unoccupied space enclosed by the spherical monomers that make up a 3D polyhedron. The latter does not include the unoccupied volume on the face of a polyhedron, which would be analogous to the unoccupied volume on the face of a disk. The relationship between interstitial volume enclosed by 3D particles and the high volume fraction

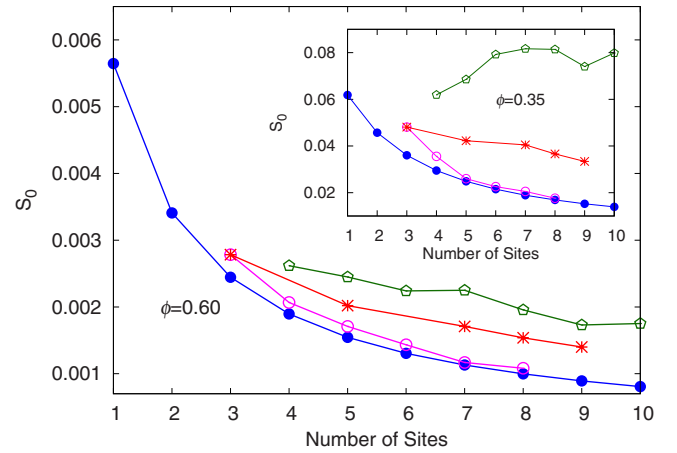


FIG. 5. (Color online) Zero-wavevector value of the collective CM structure factor (dimensionless compressibility) for rods (solid, blue circles), rings (open, pink circles), disks (red asterisks), and 3D Conway shapes (open, green pentagons) at fixed $\phi=0.60$. The inset shows the corresponding results for $\phi=0.35$.

dimensionless compressibility suggests that a suspension of hard objects which enclose a large interstitial volume is less compressible because of the trapped volume within the particles.

IV. IDEAL KINETIC GLASS TRANSITION

The CM-NMCT ideal kinetic arrest diagram for most of the shapes studied up to $N=10$ is presented in Fig. 6. As expected, the (quasi-) 1D objects form ideal glasses easiest as indicated by their critical volume fraction being the lowest. The latter monotonically decreases with number of sites or aspect ratio. The results for rings approach their rod analogs as the number of sites gets large. The planar objects have intermediate critical volume fractions which depend weakly on number of sites if N is small, with a monotonic decrease emerging at higher aspect ratio. The compact 3D shapes have the highest ideal glass volume fractions, which are larger than for a smooth sphere, and show a subtle non-

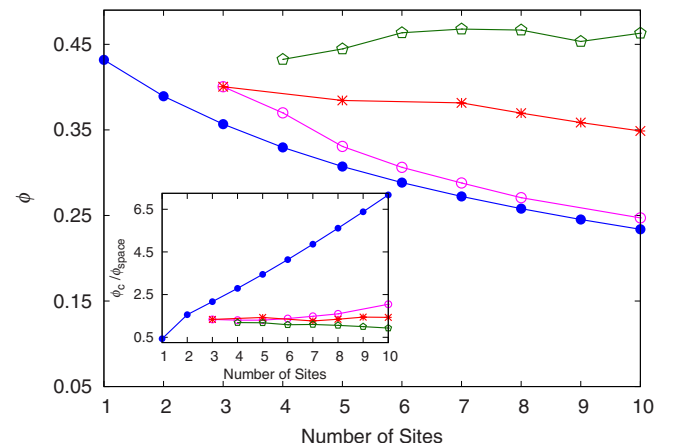


FIG. 6. (Color online) The ideal kinetic arrest diagram: The points indicate the critical volume fraction, ϕ_c , of rods (solid, blue circles), rings (open, pink circles), disks (red asterisks), and 3D Conway shapes (open, green pentagons) plotted as a function of number of sites per particle. The inset shows the ratio ϕ_c/ϕ_{space} for the same particles.

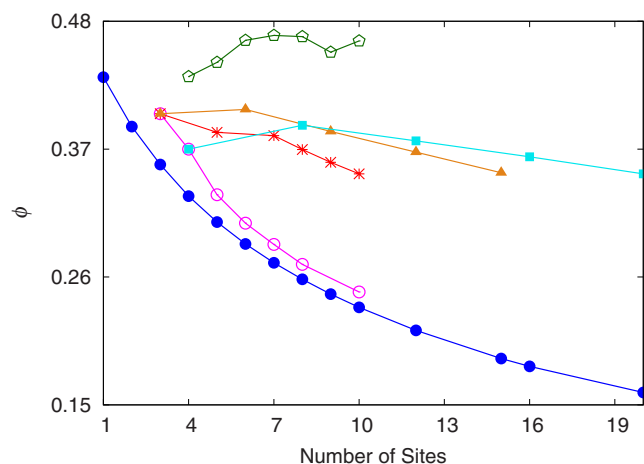


FIG. 7. (Color online) Same as Fig. 6 but the rod results are extended to $N=20$ (solid, blue circles), and the results for the triangle family (solid, light brown triangles) and square family (solid, light blue squares) are shown.

monotonic variation with N . Table I in the Appendix lists the value of the critical coupling constant, λ_c . As expected, it varies widely for different shapes.

An expanded version of the ideal kinetic arrest diagram is shown in Fig. 7 that includes rods up to $N=20$ plus the full triangle and squares families. Note that the ideal kinetic arrest volume fraction of the triangular prism and cube are significantly smaller than their more compact, R_g minimizing, counterparts. The triangle and square families both exhibit a weakly nonmonotonic variation of the critical volume fraction with N or elongation in the third dimension from the reference planar triangle and square objects, respectively. The double-stacked triangular prism is the hardest system to vitrify in analogy with the behavior of the cube for the stacked square family of shapes. It is interesting to also note that the numerical value of the onset volume fraction for both families of stacked particle shapes are comparable with that of the planar objects. At high N , the stacked triangle and square objects have mixed linear and planar character, respectively. It is notable that the ideal glass transition curves of the stacked triangle and square families cross, with the longest “triangular rod” having a lower ideal glass volume fraction than the longest “square parallelepiped” shape. For these two classes of objects the dominant surface corrugations change from those associated with the faces of triangles and squares, to those of the tangentially and linearly placed sites of a rod. The nonmonotonicity in the ideal glass transition volume fraction of these shapes mirrors the lower volume fraction dimensionless density fluctuation amplitude, as shown in Fig. 8.

Can a single particle geometric quantity be identified that organizes the diverse shape-dependent ideal kinetic arrest results? To address this question the inset of Fig. 6 plots the ratio $\phi_c/\phi_{\text{space}}$. For rods the radius of gyration grows linearly, and ϕ_{space} decays quadratically, with N . The same relationship is applicable for rings at large enough N (>10). Hence, the ideal glass transition volume fraction does not scale with ϕ_{space} for rods or rings. Rather, the linearity of the ratio for rods implies an inverse N dependence of the ideal glass transition volume fraction for rods. This trend is con-

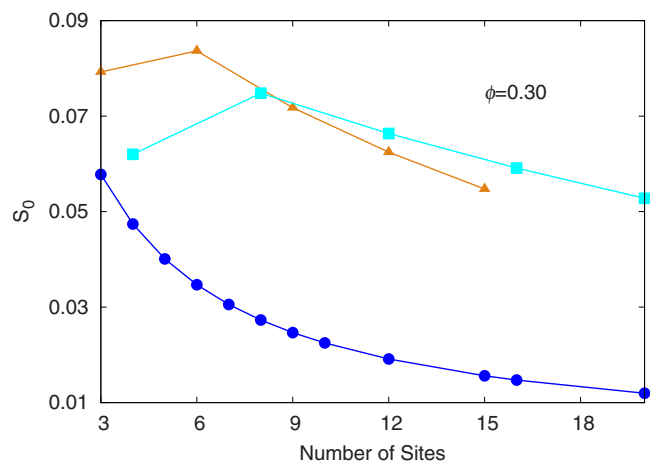


FIG. 8. (Color online) The zero-wavevector value of the CM structure factor (dimensionless compressibility) of rods (solid, dark blue circles), the triangle family (solid, light brown triangles), and square family (solid, light blue squares), at fixed $\phi=0.30$.

sistent with the well known fact³⁰ that a rod solution becomes nonideal, and can undergo a nematic phase transition, at a volume fraction of order $N\phi_{\text{space}}$. As the rings get larger, there is a hint of rodlike behavior, but finite length effects are still large for $N=3-10$.

In contrast to rods and rings, the inset of Fig. 6 shows the ideal glass transition volume fraction of the other shapes is controlled to a rough first approximation by a (nearly) universal value of the space-filling fraction. At a more detailed level there are systematic deviations, including an increase at large N for the triangle and square families which reflects the growing linear character of such prismatic and parallelepipedlike objects. Note $\phi_c/\phi_{\text{space}}$ of the Conway shapes decrease in the same manner as ϕ_{space} increases, implying particle compactness (as quantified by ϕ_{space}) is not the only determining factor of the ideal kinetic glass transition. Presumably the nature of the particle surface (roughness, corrugation) plays a role. In fact, the nonmonotonic behavior of 3D particles resembles the lower volume fraction trends of the dimensionless compressibility (inset of Fig. 5), which at higher volume fraction mirrors the behavior of the interstitial spaces within these objects. This is likely because at high volume fractions the small inaccessible intraparticle spaces become important. It is similarly possible that the lower volume fraction behavior of the dimensionless compressibility is influenced by the interstitial spaces or corrugations on the surface of nonspherical particles. If, for example, the 3D Conway shapes are considered as spheres with rough surfaces, then the deviations of both their lower volume fraction S_0 and ϕ_c from the corresponding smooth sphere values can be viewed as a function of the corrugations. This interpretation is consistent with the prior study¹⁶ of uniaxial diatomics and triatomics of different aspect ratios where the surface corrugations were varied by changing the bond length to particle diameter ratio. A nonmonotonic behavior of the ideal glass transition and compressibility was predicted as the site-to-bond length ratio is varied, and smooth spherocylinders were the hardest to vitrify.

Since each 3D Conway shape introduces a different kind

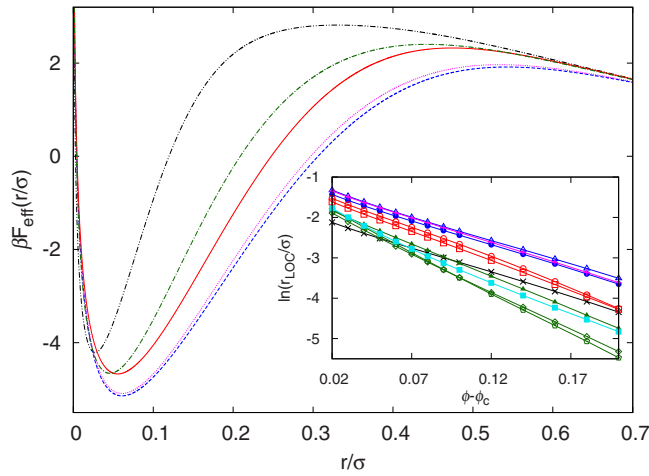


FIG. 9. (Color online) The effective free energy (units of thermal energy) as a function of CM displacement for the sphere (dotted-dotted-dashed, black curve), rod of six sites (solid, blue circles), rod of eight sites (open blue triangles), octagon (pink pluses), disk of five sites (open, red squares), disk of eight sites (solid, red curve), and snub disphenoid (dotted-dashed, green curve), at fixed entropic barrier height of $F_B=7$ kT. The inset plots the natural logarithm of the localization length in units of the site diameter as a function of the volume fraction difference variable for the sphere (black crosses), rod of six sites (solid, blue circles), rod of eight sites (open blue triangle), octagon (pink pluses), disk of five sites (open, red squares), disk of seven sites (open, red circles), tetrahedron (solid, green triangles), octahedron (open green diamonds), snub disphenoid (open, green pentagons), and cube (solid, light blue squares).

of corrugation, the ideal glass transition volume fractions (and intermediate volume fraction S_0 of Fig. 5) display a nonsystematic behavior as a function of particle size. Although there are an infinite variety of surface corrugations, our results provide evidence for surface topography of compact 3D cluster particles as an important factor in determining the tendency of these objects to undergo an ideal glass transition.

V. DYNAMICAL FREE ENERGY, LOCALIZATION LENGTH, AND SHEAR MODULUS

The dynamical free energy of Eq. (11) is a monotonically decaying function of particle displacement below the ideal glass transition volume fraction, while above it a transient localization well at $r=r_{\text{loc}}$ and barrier emerge. Examples are shown in Fig. 9 for various eight-site particles (and the smooth sphere) where volume fraction is adjusted such that the entropic barrier height is fixed at $F_B=7$ kT. The qualitative shapes of F_{eff} do not change with particle geometry; however multiple quantitative differences are evident. For example, the localization well (length) becomes narrower (shorter) and the barrier region broadens with increasing particle dimensionality. Moreover, both the localization well and barrier region broaden, and their corresponding length scales increase, as N grows.

Within NMCT, r_{loc} represents a true localization length of an ideal nonergodic state. Beyond MCT, it characterizes the displacement at which a particle is temporally trapped. The inset of Fig. 9 shows that r_{loc} is of the order of several tenths of a site diameter at the glass transition. Beyond ϕ_c , the decrease in the localization length with volume fraction is well represented as exponential. The decay becomes

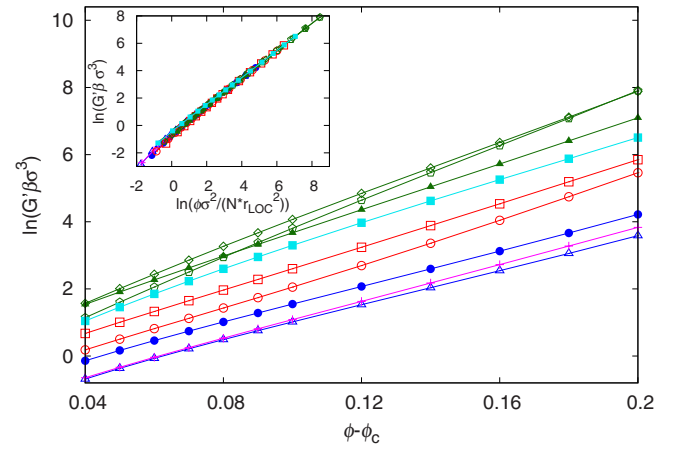


FIG. 10. (Color online) The natural logarithm of the dimensionless elastic shear modulus as a function of the volume fraction difference variable for the rod of six sites (solid, blue circles), rod of eight sites (open, blue triangles), octagon (pink, pluses), disk of five sites (open red squares), disk of seven sites (open red circles), tetrahedron (solid, green triangles), octahedron (open green diamonds), snub disphenoid (open, green pentagons), and cube (solid, light blue squares). The inset is a log-log (base 10) plot of the dimensionless modulus vs the quantity, $\phi\sigma^2/Nr_{\text{loc}}^2$, for the same particles as in the main panel.

slower with N for the 1D and 2D classes of particles, and faster with object dimensionality. The numerical results are well described by

$$\frac{r_{\text{loc}}}{\sigma} \propto e^{-a(\phi-\phi_c)}, \quad (21)$$

where $a \approx 11.9-12.5$, $11.9-12.5$, $13.9-14.9$, and $16.1-20.3$, for 1D, 2D, and 3D particles, respectively. Interestingly, the sphere shows a variation of localization length with volume fraction very similar to linear and ring objects.

A rough collapse (not shown) of all the localization lengths for 1D and 2D particles is achieved if r_{loc} is divided by the cube root of the number of sites. This suggests the localization length of noncompact particles is proportional to the length scale that defines the total volume of the object ($V_p=N\pi\sigma^3/6$) rather than the radius of gyration. However, the division of r_{loc} by $N^{1/3}$ does not collapse the 3D particle results. This is presumably because the packing efficiency of 1D and two-dimensional (fractal) objects decreases with increasing N , resulting in larger localization lengths, in contrast to compact 3D objects where the space-filling fraction depends on particle shape, not N directly. Among 3D particles of fixed N , those with smaller radii of gyration are more likely to pack efficiently, consistent with our finding that the localization lengths of octahedra and snub disphenoids are less than those of triangular prisms and cubes.

The glassy elastic shear modulus, G' , is intimately related to the localization length^{14,25} and can be described as an exponentially increasing function of the volume fraction (Fig. 10) with slopes that are modestly sensitive to particle shape. Quantitatively we find

$$G' \beta \sigma^3 \propto e^{m(\phi - \phi_c)}, \quad (22)$$

where $m=26.6-28.0$, $31.9-32.7$, and $34.3-42.3$ for 1D, 2D, and 3D particles, respectively. The rate of increase in the modulus with volume fraction monotonically softens as particle dimensionality decreases. The inset of Fig. 10 shows a dramatic collapse of all moduli when plotted versus $\phi \sigma^2 / N r_{\text{loc}}^2$. Moreover, the slope of roughly unity agrees with the analytic result of Eq. (19) that implies

$$G' \beta \sigma^3 \propto \frac{\phi}{N} \left(\frac{\sigma}{r_{\text{loc}}} \right)^2. \quad (23)$$

The maximum cage restoring force,¹⁶ which is directly related to an absolute yield stress and strain, can also be computed but is not presented here.

VI. SUMMARY AND DISCUSSION

We have extended and applied the CM version¹⁶ of NMCT to dense fluids and suspensions composed of broad families of 1D, 2D, and 3D hard nonspherical particles. The ideal MCT glass transition represents the onset of activated dynamics. Based on the MCT kinetic arrest diagram, (quasi-) 1D rods and rings vitrify at the lowest volume fraction, and increasingly so as their aspect ratio (number of sites) grows. Two-dimensional disklike objects form ideal glasses at intermediate volume fractions, which decrease with aspect ratio much more slowly than rods. Compact 3D cluster particles exhibit subtle variations of the onset volume fraction that depends on surface corrugation. The compact Conway shapes exhibit critical volume fractions larger than their non- R_g minimizing analogs. A strong correlation between the ideal kinetic arrest diagram and the dimensionless compressibility (amplitude of density fluctuations) is found. Except for 1D particles, the single particle space-filling fraction is also a good zeroth order indicator of ideal vitrification, although significant systematic deviations exist. Transient localization lengths and the shear modulus are tightly correlated, and depend exponentially on volume fraction in a manner that becomes stronger as particle dimensionality increases.

The theory as it stands can be applied to study yielding and modulus softening under applied stress, and fluids of attractive nonspherical particles³¹ that form gels or attractive glasses.³² The NMCT approach is simplified in the sense that it is based on a CM level of description which cannot describe rotational dynamics. This limitation has recently been overcome at both the NMCT and NLE levels for uniaxial objects where both CM forces and torques are present.²⁶ Encouragingly, all the basic features of the CM-based ideal kinetic arrest diagram survive. The effect of particle shape on the entropic barriers, alpha relaxation time, dynamic fragility, self-diffusion constant, kinetic vitrification, and the question of an underlying universal behavior, is studied in the following¹³ companion paper II.

ACKNOWLEDGMENTS

This work was supported by the Department of Energy, Basic Energy Sciences via Grant No. DE-FG02-07ER46471 administered through the Frederick Seitz Materials Research Laboratory.

APPENDIX: CHARACTERISTIC PARTICLE PROPERTIES

One and two particle properties of all shapes studied are summarized in Table I. In addition, the value of the coupling constant at the NMCT glass transition, λ_c defined in Eq. (16), is also listed.

TABLE I. Radius of gyration (units of site diameter), second virial coefficient (units of total particle volume), space-filling fraction, and NMCT critical coupling constant of each particle shape studied.

Shape	R_g / σ	$B_2 / \frac{\pi}{6} N \sigma^3$	ϕ_{space}	λ_c
2 rods	1	4.42	0.25	234.9
3 rods	1.32	5.35	0.164	322.8
4 rods	1.62	6.35	0.118	397.5
5 rods	1.91	7.37	0.089	463.3
6 rods	2.21	8.39	0.070	521.8
7 rods	2.5	9.42	0.056	574.7
8 rods	2.79	10.44	0.046	622.5
9 rods	3.08	11.47	0.038	665.8
10 rods	3.37	12.49	0.033	705.3
12 rods	3.95	43.58	0.024	774.7
15 rods	4.82	65.91	0.017	858.8
16 rods	5.11	74.36	0.015	883.5
20 rods	6.27	113.18	0.010	969.2
Square	1.21	4.25	0.284	446.3
Pentagon	1.35	4.80	0.254	498.8
Hexagon	1.5	5.60	0.222	554.2
Heptagon	1.65	6.44	0.194	608.06
Octagon	1.81	7.35	0.170	653.4
Decagon	2.18	9.17	0.121	745.3
Triangle	1.08	4.07	0.300	362.3
5 disks	1.32	4.37	0.269	579.7
7 disks	1.43	4.29	0.302	805.6
8 disks	1.54	4.57	0.275	891.8
9 disks	1.65	4.86	0.248	973.5
10 disks	1.72	5.10	0.244	1051.7
Tetrahedron	1.11	3.70	0.363	579.7
Triangular dipyrmaid	1.18	3.61	0.377	521.6
Octahedron	1.21	3.38	0.426	670.5
Pentagonal dipyrmaid	1.27	3.42	0.425	838.9
Snub disphenoid	1.31	3.34	0.442	987.6
Gyroelongated square pyramid	1.35	3.28	0.454	1126.1
Gyroelongated square dipyrmaid	1.36	3.26	0.497	1230.7
Triangular prism	1.26	3.64	0.372	731.4
Triply stacked triangles	1.5	8.86	0.333	1045.6
Quadruply stacked triangles	1.76	13.23	0.276	1329.7
Quintuply stacked triangles	2.03	18.51	0.225	1581.8
Cube	1.37	3.57	0.392	942.2
Triply stacked squares	1.58	11.21	0.380	1364.8
Quadruply stacked squares	1.82	16.41	0.330	1753.5
Quintuply stacked squares	2.08	22.67	0.277	2103.5

- ¹See, for example, K. L. Ngai, *J. Non-Cryst. Solids* **275**, 7 (2000); C. A. Angell, K. L. Ngai, G. B. McKenna, P. F. McMillan, and S. W. Martin, *J. Appl. Phys.* **88**, 3113 (2000); J. C. Dyre, *Rev. Mod. Phys.* **78**, 953 (2006).
- ²For reviews, see S. C. Glotzer and M. J. Solomon, *Nature Mater.* **6**, 557 (2007); A. van Blaaderen, *Nature (London)* **439**, 545 (2006); S. C. Glotzer, M. J. Solomon, and N. A. Kotov, *AIChE J.* **50**, 2978 (2004); S. C. Glotzer, M. A. Horsch, C. R. Iacovella, Z. Zhang, E. R. Chan, and X. Zhang, *Curr. Opin. Colloid Interface Sci.* **10**, 287 (2005).
- ³V. N. Manoharan, M. T. Elseser, and D. J. Pine, *Science* **301**, 483 (2003); V. N. Manoharan, *Solid State Commun.* **139**, 557 (2006).
- ⁴See, for example, E. B. Mock, H. De Bruyn, B. S. Hawkett, R. G. Gilbert, and C. F. Zukoski, *Langmuir* **22**, 4037 (2006); P. M. Johnson, C. M. van Kats, and A. van Blaaderen, *ibid.* **21**, 11510 (2005); T. Sun and Y. Xia, *Science* **298**, 2176 (2002).
- ⁵M. D. Ediger, P. Harrowell, and L. Yu, *J. Chem. Phys.* **128**, 034709 (2008).
- ⁶H. Tanaka, *Phys. Rev. E* **68**, 011505 (2003).
- ⁷W. Götze, in *Liquids, Freezing and the Glass Transition* (North-Holland, Amsterdam, 1991); W. Götze and L. Sjörgen, *Rep. Prog. Phys.* **55**, 241 (1992).
- ⁸S. Das, *Rev. Mod. Phys.* **76**, 785 (2004).
- ⁹R. Schilling, *Phys. Rev. E* **65**, 051206 (2002); C. Theis, F. Sciortino, A. Latz, R. Schilling, and P. Tartaglia, *ibid.* **62**, 1856 (2000); M. Letz, R. Schilling, and A. Latz, *ibid.* **62**, 5173 (2000).
- ¹⁰S.-H. Chong, and W. Götze, *Phys. Rev. E* **65**, 041503 (2002); **65**, 051201 (2002).
- ¹¹C. DeMichele, R. Schilling, and F. Sciortino, *Phys. Rev. Lett.* **98**, 265702 (2007).
- ¹²S. H. Chong, A. J. Moreno, F. Sciortino, and W. Kob, *Phys. Rev. Lett.* **94**, 215701 (2005); A. J. Moreno, S. H. Chong, and W. Kob, *J. Chem. Phys.* **123**, 204505 (2005).
- ¹³M. Tripathy and K. S. Schweizer, *J. Chem. Phys.* **130**, 244907 (2009).
- ¹⁴K. S. Schweizer and E. J. Saltzman, *J. Chem. Phys.* **119**, 1181 (2003); **119**, 1197 (2003).
- ¹⁵E. J. Saltzman and K. S. Schweizer, *J. Chem. Phys.* **125**, 044509 (2006); *Phys. Rev. E* **74**, 061501 (2006); **77**, 051504 (2008).
- ¹⁶G. Yatsenko and K. S. Schweizer, *J. Chem. Phys.* **126**, 014505 (2007); *Phys. Rev. E* **76**, 014505 (2007); *Langmuir* **24**, 7474 (2008).
- ¹⁷K. S. Schweizer and G. Yatsenko, *J. Chem. Phys.* **127**, 164505 (2007).
- ¹⁸D. Chandler and H. C. Andersen, *J. Chem. Phys.* **57**, 1930 (1972); D. Chandler, in *Studies in Statistical Mechanics*, edited by J. L. Lebowitz and E. W. Montroll (North Holland, Amsterdam, 1982), Vol. 8, p. 275.
- ¹⁹N. J. A. Sloane, R. H. Hardin, T. D. S. Duff, and J. H. Conway, *Discrete Comput. Geom.* **14**, 237 (1995).
- ²⁰M. Tripathy, M.S. thesis, University of Illinois, 2008.
- ²¹I. Pagonabarraga and M. E. Cates, *Europhys. Lett.* **55**, 348 (2001).
- ²²K. Miyazaki, B. Bagchi, and A. Yethiraj, *J. Chem. Phys.* **121**, 8120 (2004).
- ²³J.-P. Hansen and I. R. McDonald, *Theory of Simple Liquids*, 3rd ed. (Academic, New York, 2006).
- ²⁴T. Kirkpatrick and P. G. Wolynes, *Phys. Rev. A* **35**, 3072 (1987).
- ²⁵K. S. Schweizer, *J. Chem. Phys.* **123**, 244501 (2005).
- ²⁶R. Zhang and K. S. Schweizer, *Phys. Rev. E* (in press).
- ²⁷G. Nägele and J. Bergenholtz, *J. Chem. Phys.* **108**, 9893 (1998).
- ²⁸K. S. Schweizer and E. J. Saltzman, *J. Phys. Chem. B* **108**, 19729 (2004).
- ²⁹K. S. Schweizer, *J. Chem. Phys.* **127**, 164506 (2007).
- ³⁰G. J. Vroege and H. N. W. Lekkerkerker, *Rep. Prog. Phys.* **55**, 1241 (1992).
- ³¹M. Tripathy and K. S. Schweizer (unpublished).
- ³²V. Kobelev and K. S. Schweizer, *Phys. Rev. E* **71**, 021401 (2005); *J. Chem. Phys.* **123**, 164902 (2005).